Antenna-coupled microcavities for enhanced infrared photo-detection

Yuk Nga Chen, Yanko Todorov, Benjamin Askenazi, Angela Vasanelli, Giorgio Biasiol, Raffaele Colombelli, and Carlo Sirtori

Citation: Applied Physics Letters **104**, 031113 (2014); doi: 10.1063/1.4862750
View online: http://dx.doi.org/10.1063/1.4862750
View Table of Contents: http://scitation.aip.org/content/aip/journal/apl/104/3?ver=pdfcov
Published by the AIP Publishing

Antenna-coupled microcavities for enhanced infrared photo-detection

Yuk Nga Chen,[1] Yanko Todorov,[1,a)] Benjamin Askenazi,[1] Angela Vasanelli,[1] Giorgio Biasiol,[2] Raffaele Colombelli,[3] and Carlo Sirtori[1]
[1]*Laboratoire Matériaux et Phénomènes Quantiques, Université Paris Diderot, Sorbonne Paris Cité, CNRS-UMR 7162, 75013 Paris, France*
[2]*IOM CNR, Laboratorio TASC, Area Science Park, I-34149 Trieste, Italy*
[3]*Institut d'Electronique Fondamentale, Université Paris Sud, CNRS-UMR 8622, F-91405 Orsay, France*

(Received 7 November 2013; accepted 3 January 2014; published online 23 January 2014)

We demonstrate mid-infrared detectors embedded into an array of double-metal nano-antennas. The antennas act as microcavities that squeeze the electric field into thin semiconductor layers, thus enhancing the detector responsivity. Furthermore, thanks to the ability of the antennas to gather photons from an area larger than the device's physical dimensions, the dark current is reduced without hindering the photo-generation rate. In these devices, the background-limited performance is improved with a consequent increase of the operating temperature. Our results illustrate how the antenna-coupled microcavity concept can be applied to enhance the performances of infrared opto-electronic devices. © *2014 AIP Publishing LLC*. [http://dx.doi.org/10.1063/1.4862750]

In the mid-infrared spectral region ($5\,\mu m < \lambda < 20\,\mu m$), the performances of quantum detectors are intrinsically limited by the small energy of the electronic transition involved in photon absorption. Electrons can be thermally excited, even at low temperature, to the upper state of the transition inducing a dark current that deters the noise properties of detectors.[1] In this paper, we show that the concept of nano-antennas can be very beneficial for the improvement of their thermal performances. Nano-antennas have been actively investigated as tools to harness the interaction between quantum objects and light confined in extremely sub-wavelength regions of the space.[2–10] Here, we report on a mid-infrared detector design exploiting an array of metallic nano-antennas[11] coupled to a quantum well infrared photodetector (QWIP).[1,12] The antenna array allows the harvesting of photons from an area much larger than the device itself and compresses the electromagnetic field into sub-wavelength microcavities where the photodetection takes place.[13–15] As a result, the dark current of the detector, that is proportional to the device area, is reduced, while the photo-induced current, that is proportional to the area of collection of photons, is preserved. This geometry has a direct impact on the Background-Limited Performance (BLIP) temperature, that, as shown further, rises from 72 K for conventional QWIPs operating at 9 μm (Refs. 1, 16, and 17) to 86 K.

Our detector design, as shown in Figure 1, relies on an array of metal-semiconductor-metal microcavities with a strong sub-wavelength light confinement. According to the intersubband (ISB) selection rule, the quantum wells absorb light polarized perpendicularly to the semiconductor layers.[1] As the electric field of the fundamental cavity TM_{100} mode is dominantly polarized in the same direction, this architecture maximizes the ISB absorption and ensures contacts for the photogenerated electrons. As displayed in the images in Figure 1(a), the top metal (TiAu) has been patterned into an array of square patches of edge size s, all electrically connected by 150 nm wide wires. The period of the array is about 3 μm, much shorter than the wavelength to be detected, $\lambda \sim 9\mu m$. The absorbing semiconductor material, made of quantum wells, is inserted between a ground plane on the bottom and the metallic array on the top. Electromagnetic simulation of the electric displacement D_z of the fundamental TM_{100} mode of the structure is provided in Figure 1(b), showing strong field localization in the semiconductor

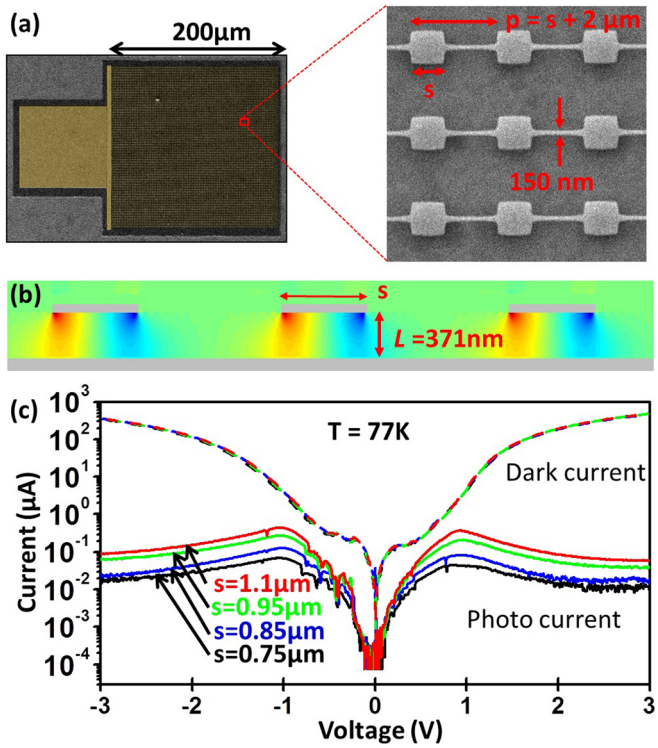

FIG. 1. Patch cavity-coupled detectors. (a) Scanning electron microscope picture of the device, with a close up of the electrically connected patch antennas. (b) Simulations of the vertical component of the displacement vector D_z of the fundamental mode of the structure. (c) Photocurrent-bias and dark current-bias characteristics of the devices with different patch sizes, at 77 K, obtained with a calibrated black body source at 500 °C under normal incidence to the grating.

[a)]Author to whom correspondence should be addressed. Electronic mail: yanko.todorov@univ-paris-diderot.fr

region.[13] The corresponding resonant wavelength is $\lambda = 2n_{eff}s$, with n_{eff} being the effective index of typical values in the range of 4.2–4.5.[18] The absorbing material is a repeat of eight 6.5 nm GaAs quantum wells cladded between 20 nm $Al_{0.25}Ga_{0.75}As$ barriers. The wells are Si-doped with sheet density 7×10^{11} cm^{-2}. The ISB transition energy between the two bound states of the well is 138 meV ($\lambda = 9.0\,\mu$m), including the depolarization shift.[19] The total thickness of the semiconductor slab is 371.5 nm, together with the top (50 nm) and bottom (100 nm) contacts Si-doped at 5×10^{18} cm^{-3}.

Microcavity detectors with different square patch sizes $s = 1.1$, 0.95, 0.85, and 0.75 μm were investigated. The modes of the cavities with $s = 1.1\,\mu$m are almost resonant with the ISB transition, while that of the other structures are progressively blue-shifted as s decreases. Figure 1(c) reports the dark current and photocurrent measurements for all the devices at $T = 77$K.[20] While the voltage-current characteristics of the dark current remain identical for all structures (Figure 1(c)), the photocurrent decreases by an order of magnitude when the cavities are detuned from the ISB transition.

In Figure 2, we show the spectra of the responsivity at 1 V (Figure 2(a)) and the reflectivity at 0 V (Figure 2(b)) obtained by illuminating the samples at 77 K under normal incidence. The responsivity has a weak dependence on the incidence angle θ and peaks at normal incidence (inset of Figure 2(a)). This angular behavior is typical of the patch-cavity arrays.[13] The responsivity spectra display a main peak at the ISB transition energy (138 meV) and a secondary feature attributed to the cavity mode that progressively blue-shifts as s decreases. This is confirmed by the reflectivity measurements (Figure 2(b)) showing that the $s = 0.75\,\mu$m cavity is detuned by about 45 meV from the ISB peak. As the cavity is brought in resonance with the ISB transition, we observe a polariton splitting of about 10 meV.[21] This phenomenon indicates the onset of the strong coupling regime,[21–23] related to the increased overlap between the electronic polarization and the tightly confined photonic mode.

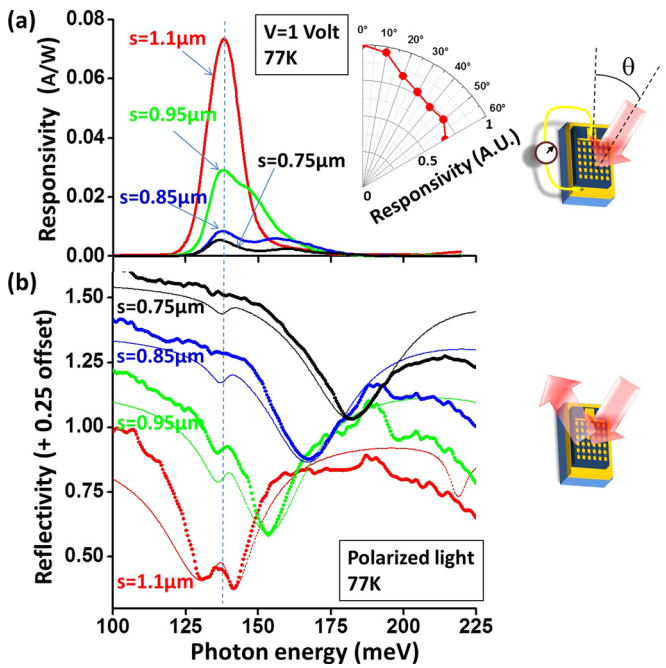

FIG. 2. Spectral characterizations of the detectors. (a) Responsivity spectra for cavities with different patch sizes at 77 K and 1 V bias, obtained with a Globar source under normal incidence. To obtain the absolute value of the responsivity, the Globar spectra were compared to that of a calibrated black body. The inset shows the variations of the responsivity of the resonant ($s = 1.1\,\mu$m) sample with the incident angle. (b) Reflectivity spectra of the samples obtained at 77 K, zero bias and with light polarized perpendicular to the connecting wire (Figure 1(a)). Bold lines are the measured spectra, while thin lines are the simulated ones.

To take into account the array and microcavity effects on the photocurrent, we have developed a model based on the electromagnetic energy conservation that provides the overall responsivity of the device

$$\mathrm{Resp}(\omega) = (1 - R(\omega))\,\frac{A_{isb}}{A_{isb} + 1/Q_{cav}}\,\frac{eg}{\hbar\omega N_{QW}}. \qquad (1)$$

Here, $\hbar\omega$ is the photon energy, g is the intrinsic photoconductive gain per quantum well,[1] Q_{cav} is the quality factor describing the cavity loss rate other than the ISB absorption (i.e., the loss at the metal and doped contact layers), and $R(\omega)$ is the reflectivity of the structure.[20] The dimensionless quantity A_{isb} is defined as $A_{isb} = (1/(\omega U))\mathrm{d}U/\mathrm{d}t|_{isb}$, where U is the total electromagnetic energy density stored in each resonator, and $\mathrm{d}U/\mathrm{d}t|_{isb}$ is the ISB absorption rate.

Equation (1) contains all the physical quantities necessary to optimize a microcavity-coupled photodetector. The first term $1-R(\omega)$ is the fraction of the incident radiation coupled inside the microcavity array. The second term is the fraction of photons absorbed per unit time in the quantum wells compared to the total optical loss. The last term is the intrinsic responsivity of the detector which depends only on the heterostructure design and the doping.[1] Clearly, the peak responsivity is optimized if the first two factors of Eq. (1) are close to 1, implying that all the impinging optical power would be coupled into the cavity and predominantly dissipated as ISB loss. This limit underlines the two main advantages of our detector design. First, each patch in the antenna array harvests all the photons impinging on an area equal to the array unit cell, $\Sigma = p^2$ (Figure 1), which is always larger than the geometrical area of the patch antenna, s^2. Since the ratio Σ/s^2 (9 in the present case) is proportional to the ratio between photocurrent over dark current, this opens the possibility to improve the detectivity and the noise limited performance of the photodetector.

The second advantage of the microcavity is that, while preserving $A_{isb} \gg 1/Q_{cav}$, the optimization of the responsivity becomes possible with few quantum wells only, contrary to the usual QWIPs.[1] The improvement of the detectivity through the increased electromagnetic confinement and better quality factors have already been exploited in photonic crystal designs;[24,25] however, in this geometry the photon collection and absorption area are very similar.

The first factor of Eq. (1) is obtained directly from the reflectivity spectra such as those shown in Figure 2(b). For the case of the resonant cavity ($s = 1.1\,\mu$m), and unpolarized light (i.e., in the same conditions as the responsivity measurements of Figure 2(a)), we obtain $1-R(\omega_{res}) = 0.50$.

For the estimate of the second term in Eq. (1), we need to quantify A_{isb} and $1/Q_{cav}$. The first quantity can be

expressed as a function of the complex dielectric function of the quantum wells $\varepsilon_{QW}(\omega)$ as $A_{isb} = f_w \mathrm{Im}(\varepsilon/\varepsilon_{QW}(\omega))$, where f_w is the overlap factor between the optical mode and the quantum wells, and ε is the static dielectric constant. In the case of a bound-to-bound transition, we have: $\varepsilon/\varepsilon_{QW}(\omega) = 1 + \omega_P^2/(\omega^2 - \tilde{\omega}_{21}^2 + i\omega\Gamma)$ with the ISB transition frequency $\tilde{\omega}_{21}$, corrected by the depolarization shift, Γ is the ISB linewidth, and ω_p is the ISB plasma frequency.[19] These parameters can be extracted from the reflectivity curves of the sample shown in Figure 2(b) (continuous lines) using the model described in Ref. 26. The position of the resonances and the shape of the curves are correctly reproduced with the nominal parameters of the sample: $\omega_p = 40$ meV, $\tilde{\omega}_{21} = 138$ meV, $f_w = 0.133$, and homogeneous broadening $\Gamma = 6$ meV. The contact layers are described by the Drude model using a doping 5×10^{18} cm^{-3} and a collision time of 60 fs, while the metal layers are modeled as in Ref. 18. These parameters provide the maximal value of A_{isb} at the ISB resonance $A_{isb}(\omega = \tilde{\omega}_{21}) = f_w\omega_P^2/\Gamma\tilde{\omega}_{21} = 0.26$. The cavity loss $1/Q_{cav}$ is extracted from the reflectivity spectra of the off-resonant cavities with $E_{peak} > 150$ meV ($s = 0.95\ \mu$m, $0.85\ \mu$m, and $0.75\ \mu$m), where we obtain, respectively, $1/Q_{cav} = 0.134$, 0.142, and 0.154. This provides an estimate of $1/Q_{cav} = 0.128$ for the resonant $s = 1.1\ \mu$m sample through linear extrapolation (assuming that $1/Q_{cav}$ varies slowly as compared to $A_{isb}(\omega)$). As a result, we obtain a branching ratio of $A_{isb}/(A_{isb} + 1/Q_{cav}) = 66\%$ at resonance, implying that a significant amount of photons coupled inside the microcavities contribute to the photocurrent generation. Note that this estimation does not take into account the mixing between the cavity and ISB losses due to polaritonic effects, which is justified since the light-matter coupling energy of 10 meV is close to the ISB absorption width, $\Gamma = 6$ meV.

For the $s = 1.1\ \mu$m resonant cavity, the fraction of photons absorbed by the quantum wells can now be estimated to be $(1 - R(\omega_{res}))A_{isb}/(A_{isb} + 1/Q_{cav}) = 0.50 \times 0.66 = 33\%$. This value, obtained here for only 8 quantum wells, is already greater than the typical absorption obtained in a multipass geometry, that is in the order of a few percent.[27,28] Knowing the corresponding peak responsivity Resp(138 meV) = 0.074 A/W (Figure 2(a)), and using Eq. (1) we extract a value of the photoconductive gain $g = 0.25$. This rather low value of the gain can be attributed to the ISB upper state being too deep below the barrier edge.[29]

To fully take advantage of the concept of microcavity detector and limit the dark current to the area under the metallic patches, where the photocurrent generation takes place, we have removed the semiconductor material in between the patches. In Figure 3, we compare the performance of the $s = 1.1\ \mu$m device before (Fig. 3(a)) and after (Fig. 3(b)) etching. In both cases, we report current-voltage characteristics of the sample, cooled at 77 K, either in the dark (dashed lines) or when the detector is exposed to a 300 K background with a field of view (FOV) of 30°. For a typical operation bias, 0.5 V, we observe that the dark current, I_{dark}, is reduced by a factor of 3, while the background current $I_{background}$ remains almost unchanged. The improvement of the ratio between $I_{background}/I_{dark}$ is evident on a very wide range of operating voltages. The reduction of the dark current is consistent with the reduction of the total device area A_D, if one

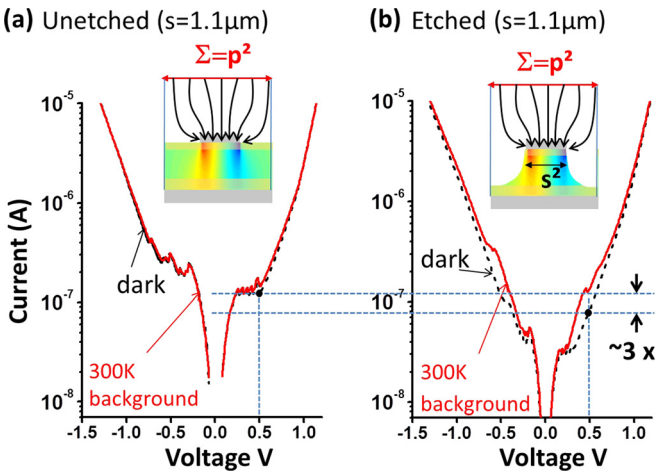

FIG. 3. Current-voltage characteristics of the $s = 1.1\ \mu$m sample before (a) and after (b) the etching of the semiconductor, at 77 K. For each case, the dark current, I_{dark}, is plotted in dashed (black) lines and the background current, $I_{background}$, in continuous (red) lines. $I_{background}$ is the current measured when the detector is exposed to 300 K illumination. The insets sketch the geometry of the sample before (a) and after (b) the etch process, together with an illustration of the Poynting flux of the wave absorbed by the antenna (lines).

takes into account the $100 \times 100\ \mu$m^2 contact pad (Fig. 1(a)). Indeed, before etching we had $A_D = 100 \times 100\ \mu$m$^2 + 200 \times 200\ \mu$m$^2 = 5 \times 10^4\ \mu$m^2, while after etching $A'_D = 100 \times 100\ \mu$m$^2 + (1/9) \times 200 \times 200\ \mu$m$^2 = 1.4 \times 10^4\ \mu$m^2, where the factor 1/9 comes from the ratio Σ/s^2 as explained above. We have $A_D/A'_D = 3.6$ that accounts well for the observed reduction of the dark current. On the contrary, the fact that $I_{background}$ is almost unchanged means that the photo-generation rate is surely not reduced, but even slightly improved in the etched devices. Indeed, the antennas still collect photons from the same effective area $\Sigma = p^2$, as illustrated in the insets of Figure 3.

In order to evaluate the impact of the reduction of the dark current on the BLIP performance of the detector, we performed systematic studies of the $I_{background}/I_{dark}$ ratio as a function of the temperature, as reported in Figure 4. For etched devices, the cavity resonance is shifted due to a slight change of the modal effective index.[20] We therefore fabricated a device with a patch size $s = 1.4\ \mu$m that becomes resonant after etching. In Fig. 4(a), we report the measured ratios $I_{background}/I_{dark}$ as a function of the temperature, and in Fig. 4(b) we show a photocurrent spectra of the $s = 1.4\ \mu$m after etching that shows only one peak, thus indicating that it has been tuned in resonance with the ISB transition.

In Figure 4(c), we plot the maximum ratio $I_{background}/I_{dark}$ measured for the $s = 1.1\ \mu$m device before and after etching, as well as for the etched $s = 1.4\ \mu$m device. No BLIP condition is observed for the unetched device. We attribute this behavior to the presence of a tunnel contribution to the dark current that dominates the transport at low temperature.[30] In the case of the etched devices, we observe a BLIP temperature of 83 K for the $s = 1.1\ \mu$m device and 86 K for the $s = 1.4\ \mu$m device in the negative bias, much higher than the BLIP temperature of 72 K reported in the substrate coupled configuration for optimized QWIP operating at 9 μm.[1,16,17] This significant improvement of the BLIP temperature illustrates once again the fact that in our

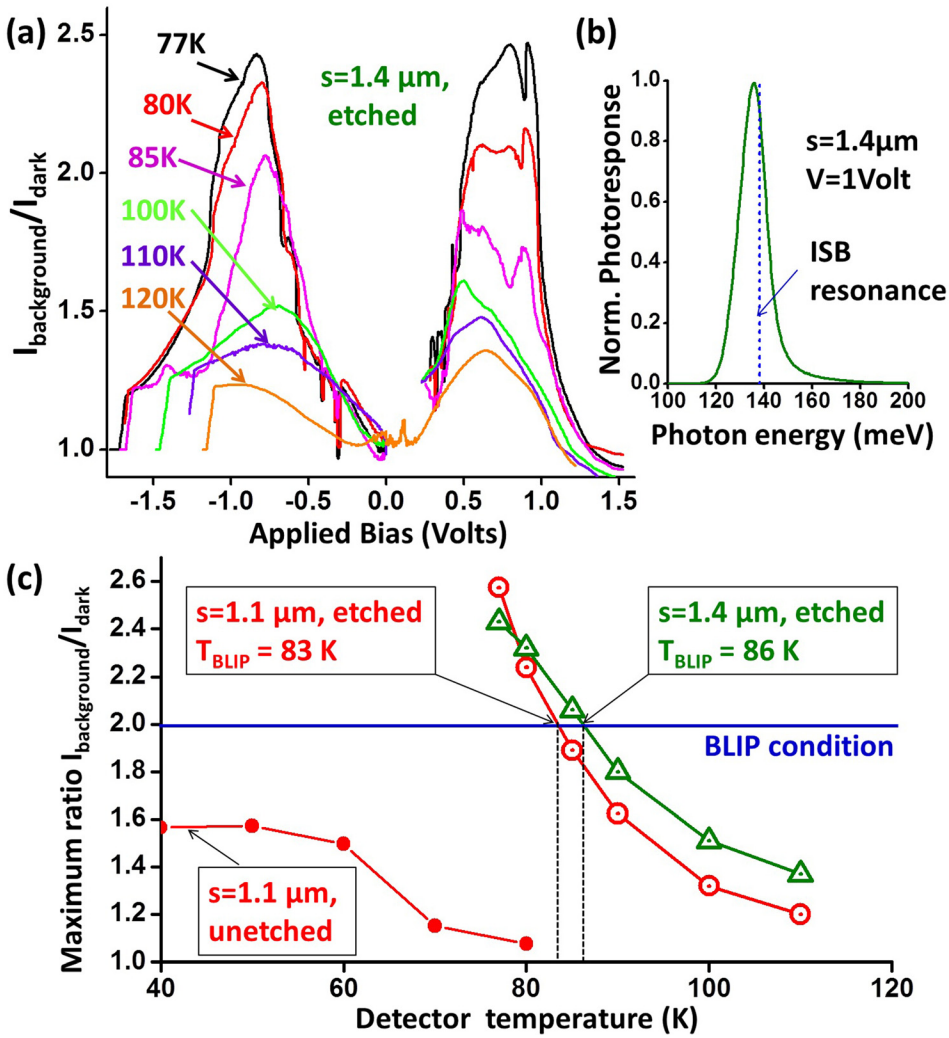

FIG. 4. (a) Measurements of the ratio $I_{background}/I_{dark}$ as a function of the bias at different temperatures for the etched $s = 1.4\,\mu m$ sample. As shown in the photo-response spectrum (b) this sample becomes resonant with the ISB absorption after etch. (c) Evolution of the maximum ratio $I_{background}/I_{dark}$ as a function of the detector temperature of the etched and unetched devices. The circles correspond to the $s = 1.1\,\mu m$ sample and the triangles to the $s = 1.4\,\mu m$ sample, the dots correspond to the $s = 1.1\,\mu m$ sample before etch. The horizontal line indicates the BLIP condition $I_{background}/I_{dark} = 2$.

antenna-based design the effective area that contributes to the photocurrent (signal) can be made larger than the area contributing to the dark current (noise). Furthermore, the light collection can be still optimized with a proper design of patch microcavity arrays, which will enable to push the system to the critical coupling regime, where $R(\omega_{res}) \sim 0$ and all incident photons are absorbed in the structure.[13]

In conclusion, we have demonstrated antenna-coupled microcavity QWIP. This geometry brings important degrees of freedom in the design of infrared photodetectors, as it allows for an efficient light funneling into the active region, independent of the incident angle and polarization. Potentially, this concept will lead to an ultimate detector containing only one quantum well, while absorbing almost all of the incident radiation to generate photocurrent.

We gratefully acknowledge financial support from the ERC grant "ADEQUATE." We acknowledge technical help from Maria Amanti on the dry etch of the samples.

[1]H. C. Liu, *Intersubband Transitions in Quantum Wells: Physics and Device Applications*, edited by H. C. Liu and F. Capasso (Academic Press, San Diego, 2000).
[2]C. Belacel, B. Habert, F. Bigourdan, F. Marquier, J.-P. Hugonin, S. Michaelis de Vasconcellos, X. Lafosse, L. Coolen, C. Schwob, C. Javaux, B. Dubertret, J.-J. Greffet, P. Senellart, and A. Maitre, Nano Lett. **13**, 1516 (2013).
[3]A. Kinkhabwala, Z. Yu, S. Fan, Y. Avlasevich, K. Mullen, and W. Moerner, Nat. Photonics **3**, 654 (2009).
[4]P. Biagioni, J. S. Huang, and B. Hecht, Rep. Prog. Phys. **75**, 024402 (2012).
[5]A. Curto, G. Volpe, T. Taminiau, M. Kreuzer, R. Quidant, and N. van Hulst, Science **329**, 930 (2010).
[6]T. Taminiau, F. Stefani, F. Segerink, and N. van Hulst, Nat. Photonics **2**, 234 (2008).
[7]L. Novotny and N. van Hulst, Nat. Photonics **5**, 83 (2011).
[8]P. Mühlschlegel, H.-J. Eisler, O. J. F. Martin, B. Hecht, and D. W. Pohl, Science **308**, 1607 (2005).
[9]N. Liu, M. Mesch, T. Weiss, M. Hentschel, and H. Giessen, Nano Lett. **10**, 2342 (2010).
[10]A. Cattoni, P. Ghenuche, A.-M. Haghiri-Gosnet, D. Decanini, J. Chen, J.-L. Pelouard, and S. Collin, Nano Lett. **11**, 3557 (2011).
[11]C. Feuillet-Palma, Y. Todorov, A. Vasanelli, and C. Sirtori, Sci. Rep. **3**, 1361 (2013).
[12]B. F. Levine, K. K. Choi, C. G. Bethea, J. Walker, and R. J. Malik, Appl. Phys. Lett. **50**, 1092 (1987).
[13]Y. Todorov, L. Tosetto, J. Teissier, A. Andrews, P. Klang, R. Colombelli, I. Sagnes, G. Strasser, and C. Sirtori, Opt. Express **18**, 13886 (2010).
[14]A. Delteil, A. Vasanelli, Y. Todorov, C. Feuillet Palma, M. Renaudat St-Jean, G. Beaudoin, I. Sagnes, and C. Sirtori, Phys. Rev. Lett. **109**, 246808 (2012).
[15]L. Le Perchec, Y. Desieres, and R. Espiau de Lamaestre, Appl. Phys. Lett. **94**, 181104 (2009).
[16]S. Gunapala, S. Bandara, J. Liu, E. Luong, S. Rafol, J. Mumolo, D. Ting, J. Bock, M. Ressler, and M. Werner, Infrared Phys. Technol. **42**, 267 (2001).

[17]S. Gunapala, S. Bandara, A. Singh, J. Liu, E. Luong, J. Mumolo, and P. LeVan, Physica E **7**, 108 (2000).
[18]P. Jouy, Y. Todorov, A. Vasanelli, R. Colombelli, I. Sagnes, and C. Sirtori, Appl. Phys. Lett. **98**, 021105 (2011).
[19]T. Ando, A. Fowler, and F. Stern, Rev. Mod. Phys. **54**, 437 (1982).
[20]See supplementary material at http://dx.doi.org/10.1063/1.4862750 for the details of the measurements, details of the derivation of Eq. (1), and experimental details with etched samples.
[21]P. Jouy, A. Vasanelli, Y. Todorov, A. Delteil, G. Biasiol, L. Sorba, and C. Sirtori, Appl. Phys. Lett. **98**, 231114 (2011).
[22]Y. Todorov, A. Andrews, R. Colombelli, S. De Liberato, C. Ciuti, P. Klang, G. Strasser, and C. Sirtori, Phys. Rev. Lett. **105**, 196402 (2010).
[23]L. Sapienza, A. Vasanelli, C. Ciuti, C. Manquest, C. Sirtori, R. Colombelli, and U. Gennser, Appl. Phys. Lett. **90**, 201101 (2007).
[24]W. Wu, A. Bonakdar, and H. Mohseni, Appl. Phys. Lett. **96**, 161107 (2010).
[25]S. Kalchmair, R. Gansch, S. I. Ahn, A. M. Andrews, H. Detz, T. Zederbauer, E. Mujagić, P. Reininger, G. Lasser, W. Schrenk, and G. Strasser, Opt. Express **20**, 5622 (2012).
[26]Y. Todorov, L. Tosetto, A. M. Andrews, A. Delteil, A. Vasanelli, G. Strasser, and C. Sirtori, Phys. Rev. B **86**, 125314 (2012).
[27]A. G. Steele, H. C. Liu, M. Buchanan, and Z. R. Wasilewski, J. Appl. Phys. **72**, 1062 (1992).
[28]G. Hasnain, B. Levine, S. Gunapala, and N. Chand, Appl. Phys. Lett. **57**, 608 (1990).
[29]H. Schneider and H. C. Liu, *Quantum Well Infrared Photodetectors: Physics and Applications* (Springer, Berlin, 2007).
[30]V. Trinité, E. Ouerghemmi, V. Guériaux, M. Carras, A. Nedelcu, E. Costard, and J. Nagle, Infrared Phys. Technol. **54**, 204 (2011).